Quantitative Morphology of Bedrock Fault Surfaces and Identification of Paleo-earthquakes

He Honglin[1], Wei Zhanyu[1], Alexander Densmore[2]

1 Key Lab. of Active Tectonics and Volcano, Institute of Geology, China Earthquake Administration, Beijing 100029

2 Department of Geography and Institute of Hazard, Risk and Resilience, Durham University, Durham DH1 3LE, UK

Abstract The quantitative analysis of morphologic characteristics of bedrock fault surfaces may be a useful approach to study faulting history and identify paleo-earthquakes. It is an effective complement to trenching techniques, especially to identify paleo-earthquakes in a bedrock area where trenching technique cannot be applied. In this paper, we calculate the 2D fractal dimension of three bedrock fault surfaces on the Huoshan piedmont fault in the Shanxi Graben, China using the isotropic empirical variogram. We show that the fractal dimension varies systematically with height above the base of the fault surface exposures, indicating a segmentation of the fault surface morphology. We interpret this segmentation as being due to different exposure duration of parallel fault surface bands, caused by periodical earthquakes, and discontinuous weathering. We take the average of fractal dimensions of each band as a characteristic value to describe its surface morphology, which can be used to estimate the exposure duration of the fault surface band and then the occurrence time of the earthquake that exposed the band. Combined with previous trenching results, we fit an empirical relationship between the exposure duration and the morphological characteristic value on the fault: $D = 0.049\ T + 2.246$. The average width of those fault surface bands can also be regarded as an approximate vertical coseismic displacement of characteristic earthquake similar to the Hongdong M8 earthquake of 1303. Based on the segmentation of quantitative morphology of the three fault surfaces on the Huoshan piedmont fault, we identify three earthquake events. The coseismic vertical displacement of the characteristic earthquake on the Huoshan piedmont fault is estimated to be 3-4 m, the average width of these fault surface bands. Gaps with a width of 0.1-0.3 m between two adjacent bands, in which the fractal value increases gradually with fault surface height, are inferred to be caused by weathering between two earthquakes or interseismic slip on the fault.

Keywords: Morphology of bedrock fault surface, Paleo-earthquake, Isotropic empirical variogram, Huoshan piedmont fault

1 Introduction

Seismic risk evaluation of active fault zones is mainly based on the seismic records, including both historical and pre-historical earthquakes (Wallace, 1981), a reasonable seismic risk evaluation then mainly relies on the integrity of seismic records (Parsons et al., 2000). Due to the lack of sufficiently long historical or instrumental seismic data sets, paleoseismic investigations aimed to identify paleo-earthquake preserved in the geological and geomorphic records is necessary to prolong seismic records (McCalpin, 2009). Trenching is an important technique widely applied to the paleoseismology and has achieved outstanding results (e.g. Young et al., 2002; Ran et al., 2010；Galli et al., 2008), as can often identify past major earthquakes that have ruptured the ground surface at a particular site. However, this method has some weaknesses; for example, interpretation of offset strata and fault-rupture related features is sometimes debatable, and suitable offset materials that can be dated are required to bracket the event times, usually leaving large uncertainties (e.g. Hilley and Young, 2008). Moreover, it can be applied to a fault in bedrock site only in selected cases (Galli and Bosi, 2003; Galli et al., 2006; 2012; Galli and Peronace, 2014). Therefore, it is necessary to seek some other techniques to study paleoseismology on faults in bedrock.

Bedrock fault scarps may be interpreted as the cumulative result of repeated surface faulting in many active tectonic terrains, and potentially preserve a valuable paleoseismic record (Mayer 1984; Stewart, 1993). In the last decade, bedrock fault scarps have become an attractive complement for paleoseismological studies because the exposure duration of a bedrock fault scarp can be inferred by methods based on the accumulation of cosmogenic nuclides (Zreda and Noller, 1998; Benedetti et al., 2000; Mitchell et al., 2001). Nevertheless, if one want to infer both the age and slip of the last few major earthquakes on the fault using the cosmogenic nuclides technique to a bedrock fault surface, hundreds of samples should be taken continuously on the bedrock fault surface (e.g. in Schlagenhauf A., 2009). This is a very expensive work both in manpower and material.

Geologists have noted long before that the features of the bedrock surfaces gradually changed in texture or roughness with exposure duration due to external influences and several geomorphic process (i.e. weathering, karstification, bioerosin) when the fault surface are exposed. As a result, abrupt changes in the features of fault surfaces may appear as parallel bands on the same fault surface exposed in different times. Sharp weathering contrast on fault surface has been used to delimit recent exposure increments through visual observation in field (e.g. Wallace 1984, Stewart, 1993), or through photographic study (Giaccio et al., 2002), but without conclusive results. Recently, terrestrial laser scanning (t-LiDAR) has been widely applied to acquire accurate morphologic features of bedrock fault surfaces in neotectonic and geological earthquake studies (e.g. Sagy et al., 2007; Candela et al., 2009; Brodsky et al, 2011; Renard et al., 2012). Few use of t-LiDAR has been undertaken to characterize the weathered fault surface and identify sequentially exposed bands on fault surfaces (e.g. Wei et al., 2013). Only recently, through t-LiDAR data Wiatr et al. (2015) suggests evidences for repeated faulting of the Pisia fault, Greece, with 30-60 cm of displacement at one site based on the fact that the roughness increases with scarp height on naturally exhumed bedrock fault scarps.

Previous studies of bedrock fault surface with t-LiDAR have shown that the morphology of fault surfaces is self-affine and fractal. Fractal dimension is suitable to characterize the roughness in various scale for t-LiDAR data of bedrock surfaces (reviewed in Candela et al., 2009). Our approach applies the fractal analysis on the natural bedrock fault surface to identify possible weathered bands of fault surface which can be related to seismically-exhumed fault surface, and then identify paleoseismic events. Besides identifying differently weathered bands, another important purpose of our research is searching for mathematic model to relate the digital morphologic feature of fault surface to the exposure duration, which has not been done by previous research works. Therefore, it is necessary to quantify the morphology of bedrock fault surface using a special mathematic method fitting to weathering feature. It is the groundwork not only to identify differently weathered bands of paleoseismological interests but also to relate the digital morphologic feature of fault surface to the exposure duration. For this aim, we focus here on the Huoshan piedmont fault (HF), which is an active normal fault extending along the eastern boundary of the Shanxi Graben, China (Figure 1). The M 8.0 Hongdong earthquake of 1303 was produced by the fault, and several other destructive earthquakes have been disclosed by trenching (Xu and Deng, 1990; Xu, 2013). Moreover, along the fault zone there are a lot of fault scarps, which supply plentiful samples to be selected to our research.

Firstly, we scan three bedrock fault surfaces with a t-LiDAR. Secondly, we describe the fault surface morphology by its fractal dimension as calculated by the isotropic empirical variogram method and a cellular fractal model. We ascribe the characteristic morphologic fractal values of each fault surface band to individual earthquake events, and analyze the relationship between the fault surface morphology and the exposure duration, and further paleoseismologic information recorded in the bedrock fault surface.

2 Target fault and 3D data of fault surface

2.1 Seismotectonic framework

The HF, located on the eastern flank of the central Shanxi Graben at the eastern boundary of the Ordos block, China (Figure 1a, b), is an active boundary fault between the Huoshan Range and its piedmont basin. It extends 116 km to the NNE from Subao town, Hongdong county to Longfeng town, Jiexiu county, and dips to the NW at 65-75° (Xu et al., 2011). In the footwall, the Huoshan Range is an asymmetrical tight anticline with a core of Archean gneiss. Since the Pliocene, this anticline has been tilted along the fault forming a fault block mountain. The hanging wall is filled by sediments that range from Pliocene to Late Pleistocene (Figure 1c). Previous research demonstrated that active faulting occurred from the end of the Pliocene through the Holocene (Xu and Deng, 1990; Zhang et al., 1998; Wen, 2000; Xie et al., 2004). The HF has been identified as the seismogenic fault responsible for the 1303 M 8.0 Hongdong earthquake (Figure 1b), which is the first M 8 earthquake hypothesized from historical descriptions in China (Liu and Meng, 1975; Wang et al., 1996). The HF is marked by well-developed triangular facets and bedrock fault scarps caused by dominantly normal-slip faulting. Trenching investigation on the southern segment of the HF found 4 paleo-earthquakes (Xu and Deng, 1990; Xu, 2013). The oldest one occurred between 28580-26380a BP, whereas, the other three occurred in the Holocene, 4620-5455a BP, 2555-3475a BP and the 1303 M 8.0 Hongdong earthquake, showing an average recurrence interval of about 2000a.

We chose to focus on three bedrock fault surface exposures near Liwan town (Huozhou city, Figure 1c), which are all located in the epicentral area of the 1303 Hongdong earthquake, and are all carved on Archean gneiss of the Huoshan fault footwall. Therefore, the three fault surfaces have similar faulting histories and are likely to have similar weathering resistance.

Field observation also found several weathered horizontal bands on fault surfaces, different morphologic features in different height due to different weathering degree. The fault surface presents smooth with some striations and steps on the bottom due to faulting, rough with some weathered pits and grid fissures on the middle, more rough and more wide cracks due to erosion and plant root growth on the upper, while on the top of the fault scarp covered by weathered debris and shrub.

2.2 Scanned fault surface and Data Acquisition

We scanned the three fault surfaces (Figure 2) using a t-LiDAR, a Trimble GX 3D (Figure 2, upper of c), which is an automatic survey instrument with high resolution and a 300 m maximum scan radius, and the space between two adjacent scan points ranges from 1.6 mm to 5 mm according to the distance between the scanner and the fault surface from 5 m to 300 m. We scanned only those areas of the fault surface with no vegetation or sediment cover. The scan results are three point clouds in which each scan point is described by its 3D geometric coordinates, and average space between adjacent points is 2 mm across the three point clouds. We interpolated the scan data into a DEM with an equal cell size of 2 mm using natural neighbor method (Figure 2). The lower three of Figure 2 show the morphology of the three scanned fault surface DEMs derived from the point clouds.

3 Study methods

3.1 Fractal dimension characterizing the surface roughness

Assuming that our fault has been exhumed mainly by coseismic slip, the surface observed features are likely produced by the combination of two mechanical processes: faulting abrasion, and post-earthquake weathering and erosion. Faulting abrasion is expected to make the morphology of fault surface more anisotropic, so that the roughness in the direction parallel to slip becomes less than that in the direction perpendicular to slip (Sagy et al., 2007). Conversely, weathering is expected to be a more random process, and makes the fault surface more isotropic and rougher. Previous studies, emphasizing the impact of faulting abrasion on the fault surfaces, often used the power spectral density (Power et al., 1988; Power and Tullis, 1991; Brown, 1987) and standard deviation (Renard et al., 2006; Candela et al., 2009) to describe the roughness based on line profiles parallel or perpendicular to slip. These 1D analysis methods are useful to explore the relation between fault surface morphology and faulting processes (Power et al. 1987; Sagy et al., 2007, 2009; Wei et al., 2010), but not for understanding the effects of weathering on morphologic characteristics, because the weathering is a random and isotropic process on two-dimensional surface. Moreover, t-LiDAR allows genuinely two-dimensional data of fault surface to be gathered, typically in the form of digital images. Such data offer exciting opportunities for addressing issue of spatial variation in a way that is difficult for line transects of surface.

Because the fractal dimension can capture the essence of a natural surface roughness (Viewed in Burrough, 1981; Mandelbrot, 1983), it has been widely used in earth sciences for textural analysis of topography and characterizing geological quantities of Earth (Polidori et al., 1991; Klinkenberg and Goodchild, 2002; Sung and Chen, 2004). The surfaces of rocks associated with slip wear, weathering and erosion is similar to the real landscapes which have statistical properties similar to fractional Brownian surface (Brown, 1987), it is possible to describe the roughness of the fault surface using the fractal dimension (e.g., Sage et al., 2007; Candela et al., 2009). Isotropic empirical variogram proposed by Davies and Hall (1999) is an effective method to estimate the fractal dimension of 2D spatial data (Gneiting et al., 2012). Therefore, here we calculate the 2D fractal dimension using a cellular fractal model and the isotropic empirical variogram to quantitatively describe the weathering morphology of fault surface.

3.2 Calculation of two-dimensional fractal

The isotropic empirical variogram, i.e., the statistical variation of mean differences with distances between two points, is an extension of the Hausdorff dimension in a two-dimensional random field (Davies and Hail，1999). Taking X as a random process (one dimension series) or random field (two dimensional plane), $\gamma(t) = \mathrm{cov}\{X(t), X(0)\}$ is the covariance of a pair of points with separation distance t. Generally, there is a relationship between the $\gamma(t)$ and the separation distance (t) as follows:

$$\gamma(t) \propto c||t||^{\alpha} \qquad (1)$$

where α is the fractal index, which is between 0 and 2. There is a linear relationship between the fractal index (α) and fractal dimension (D) as follows:

$$D = d+1-\alpha/2 \qquad (2)$$

where d is the topological dimension of the data field. For random processes d is equal to 1, and for random fields d is 2. The fractal dimension (D) can be calculated by α which is the slope of the best-fitting line based on the double logarithmic linear regression of the isotropic variogram (Equation 1) shown in Figure 3. The cellular fractal model following Sung et al (1998), a moving window operation (Figure 4), is used to calculate the fractal dimension distribution on the fault surface in this paper. The moving window traverse the entire fault surface with the offset for each move in directions of horizontal and vertical to calculate the fractal dimension using the variogram method. The moving window is defined to N×N (cells of DEM), then the offset for each move is N/2 (Figure 4a). The area within each window can be treated as a homogeneous unit and is described by a uniform fractal dimension which can be derived by double logarithmic linear regression of Equation 1. A raster image of fractal dimension is made to display the spatial distribution of roughness on a surface, and the resolution of raster data is N/2, the offset of the window (Figure 4b). The surface units within moving windows at the same height likely experienced the similar faulting abrasion and weathering erosion, and their fractal dimension values display a normal distribution. To characterize differences in natural fault surface alteration along the height of the fault surface, we calculated the mean value with 95% confidence interval of the normal population for each horizontal row in raster image of fractal dimension. The average fractal along the surface height is then used to evaluate the disparity of the fault surface topography.

3.3 Choice of the moving window

The proper size of the window is very important to both the accuracy and the precision of fractal dimension using variogram (Sung et al., 1998). Too small windows cover insufficient data and increase the uncertainty of the fractal dimension estimate; too large windows increase the changes of capturing heterogeneous and multi-fractal characteristics within the window and decrease the spatial resolution of the fractal dimension. Sung et al. (1998) found that the percentage of acceptable fractal dimension estimations for three synthesized surfaces decreases with a decreasing window size. It drops drastically if the window size is smaller than 30×30. They suggested that 30×30 is the smallest data matrix that provides >80% of the accurate estimate of the surface fractal dimension, and there is little difference in the estimator of fractal dimension when the window size is larger than 60×60. This technique has been applied for quantifying the heterogeneity of various surfaces, such as sea floor (Wilson et al., 2007), landform (Bi et al., 2012) and bedrock surface (Wiatr et al., 2015). We chose three types of the moving window, 32×32, 64×64 and 128×128 in grid, to calculate the 2D fractal dimensions of the three bedrock fault surfaces. Because the grid spacing of the morphologic DEM is 2 mm, the sizes of three windows are 64×64 mm^2, 128×128 mm^2 and 256×256 mm^2, respectively. Based on the supposed coseismic vertical displacement of AD 1303 earthquake, these window sizes are significantly smaller than the displacements which control the abrupt changes in the features of fault surfaces.

4 Results and interpretation

The raster images in figure 5 show the spatial distribution of two-dimensional fractal values on the scanned fault surfaces. Because our primary objective is to reconstruct the past seismic slip history of bedrock fault scarps, we are more interested in the vertical changes (dip changes) of roughness along the fault surface. However, the raster image of fractal show faint variations of the fractal dimension, without a clear trend as a function of the fault height. As a result, it is not easy to identify the presence of bands characterized by different weathering degree along the surface height in such raster images (figure 5). Therefore, averaging the fractal values of each horizontal row (perpendicular to dip) in raster image was performed in order to determine the roughness changes along the height of the fault surface. Through viewing the plots of average fractal against surface height, a stair-like increase can be recognized on the analyzed surface from base to top, with values ranging from 2.2 to 2.7. (i.e., the base of the fault surface is smoother with low fractal value, and the top is rougher with high fractal value). Such changes in roughness along fault surface is similar to the changes in the amount of specific cosmogenic isotopes along seismic exhumed bedrock scarps (e.g. Schlagenhauf et al., 2010), which allow to use the surface roughness to provide earthquake information from bedrock fault scarps.

“Stair-like” increase in the surface roughness with increasing scarp height has originally been described by Wallace (1984) and Stewart (1996) for seismic exhumed bedrock fault scarps. These authors first proposed a mechanism that may have produced such roughness fluctuations: Before being exposed above ground level by an earthquake, the bedrock fault surfaces had been smoothed by sliding wear during faulting actives. Faults generally emerge from the ground as smooth, polished planes. Once exposed above ground level by an earthquake, the scarp rock begin to be roughened by the weathering processes which leads to increased rock surface roughness with time (Giaccio et al., 2002; Galli et al., 2010; Wei et al., 2013). One band on a fault surface exhumed by an earthquake experienced the same weathering processes under similar sub-aerial conditions, thus, it would have the same roughness. As bedrock scarps are progressively exhumed by the action of repeated large earthquakes, the roughness along the entire exposed scarp should take a “stair-like” curve made of a series of approximate straight sections separated by sharp discontinuities. The vertical separation between two successive discontinuities provides a measure of the displacements produced by the earthquakes.

5 Discussions

5.1 Determination of weathering bands along surface

Identification of bands is a decisive step as far as the seismic intensity, the seismic cycle and seismic hazard assessment are concerned (Schlagenhauf et al., 2010; Mouslopoulou et al., 2011). Through visual identification in the plots of average fractal versus scarp height (Figure 5), there are three obvious bands for surface A and surface B, and two bands for surface C. In addition to the visual identifications, a statistical analysis was used to validate these bands with different roughness on a scanned fault surface (i.e., Student's t-test. See details and results in the Supplementary materials).

The result of Student’s *t*-test, similar to the visual interpretation, show that there are three bands for surface A and B, and two bands for surface C, but with a more robust statistical evidence for band division. For surface A, two discontinuities in surface roughness are located at the height of 0.9–1.2 m, 5.1-5.3 m, respectively: for surface B, two discontinuities are located at the height of 1.5-1.8 m, 5.8-5.9 m, respectively; surface C has only one discontinuity in roughness located at the height of 1.1-1.3 m. We also found some tiny fluctuations in the mean fractal curves (Figure 6) that may be caused by the local slight difference in rock constituents along fault surface or noise data from t-LiDAR measurement. Therefore, we do not think those tiny fluctuations can act as a discontinuity in roughness.

According to the band division above, we calculated the mean and the standard deviation of fractal dimension for each surface band, and the results are summarized in table 1 and showed by the red lines in Figure 5. These mean values can be seen as the characteristic fractal dimensions for bedrock fault surface bands, and as a morphologic parameter characterizing the surface roughness to quantify the degree of weathering.

5.2 Paleoseismic events and coseismic slips

Under the hypothesis that the weathered bands of fault scarp are the result of repeated fault slip events, our three bands would indicate three slip events. Historical earthquake analyses and paleoseismic investigations along the HF have indicated that three surface-rupturing earthquakes occurred during the Holocene (Xu and Deng, 1990; Xu, 2013), which is consistent with our paleoseimic result demonstrated via differential weathering on fault surfaces. Therefore, these three bands from bottom to top match the three earthquakes dated 1303, 2555-3475 a BP and 4620-5455 a BP.

As the upper and lower extents of the surfaces were not scanned completely, we cannot usethese surface segments to estimate the vertical co-seismic displacement.Conversely, the middle segments of surface A and B had been scanned completely, and their width of about 4 m quite possibly represent the dip-slip offset of the penultimate earthquake. Considering the fault dip of 75°, the vertical co-seismic displacement during the penultimate earthquake is 3.8 m. Compared to the vertical co-seismic displacement offor the Hongdong earthquake of 1303 (4-5 m), the vertical co-seismic displacement of 3.8 m implies that the penultimate earthquake had a similar magnitude with the Hongdong earthquake. Wei et al. (2015) used faulting knickpoints to indicate that the ruptures on the HF obey a characteristic slip model with a similar slip (about 4

m) for several successive earthquakes as well. Moreover, between two adjacent weathered bands, there is a narrow gap, the fractal value of which increases gradually with fault surface height. The two possible explanations for the formation of the gap are an inter-seismic creep slip along the fault, or a gradual erosion along the base of the fault scarp for a long time.

We made an evolutionary model of fault scarp surface in bedrock (Figure 7), where the fault scarp has been divided into two main sections according to the dip angle and weathering degree. The upper section has seriously been weathered, its dip angle has changed to be lower than the original fault dip angle; the lower section has not been weathered so much and some faulting abrasion feature has been saved, and its dip angle has been kept to be similar to the original fault dip angle. We can identify the weathering band by naked eye according to large scale morphological feature and dip angle variation in the upper section. In the model, there are two surface morphological bands with different weathering degree in the upper section identified by naked eye, and three surface morphological bands in the lower section identified by roughness analysis based on high-resolution DEM measured by t-LiDAR. These five surface morphological bands with different weathering degree might correspond to five earthquake faulting events.

5.3 Weathered characteristics as a function of exposed time of the fault surface

In order to make fractal index a reliable palaeoseismological tool, it should be understand how the fractal indices of fault surface changes over the exposure time, that is, what is the relationship between the fractal index and the exposed time of the fault surface.

To build such relationship, we need in advance two variables: one is the fractal index quantifying the degree of weathering, and another is the exposure time . In our case, the youngest event can be dated at 1303 AD by historic documents, and other two paleoearthquakes were dated at 2555-3475a BP and at 4620-5455a BP, respectively, by means of paleoseismological trenching (Xu et al., 1993). In Figure 8 we plotted the characteristic fractal dimensions *vs* the occurrence times of supposed paleo-earthquakes, i.e. the exposed time of surfaces segments, for surface A, Surface B and the set of studied surfaces. There seem to be an ascending linear trend of fractal value with the exposed time of fault surface (dashed lines in Figure 8).

$$D = 0.049\ T + 2.246 \qquad (3)$$

where D is the fractal dimension, and T is the exposed time of fault surface which unit is ka. As we know that the two-dimensional fractal has an upper limiting value of 3, this will gradually approach a steady value over the exposed time when the morphology of bedrock fault surface reaches the equilibrium with the weathering and erosion on surface. As a result, the relationship between the characteristic fractal dimensions and the exposed time should be nonlinear and complicated in a long enough time scale. At present, however, we do not know more information about this relationship. Our result revealed the linear trend between the characteristic fractal dimensions and the exposed time ranging from 0.7 ka to 5 ka on studies fault surfaces (Equation 3). We speculate that the relationship between the characteristic fractal dimensions and the exposed time can be treated as a linear function approximately in a centennial-millennial scale. However, to obtain a more accurate relationship, the changes of fractal dimension over a much larger time scale are necessary. Therefore, it is one of our important research targets in future that the weathering stability and weathering behavior of the various lithologies on the bedrock fault.

6 Conclusions

The quantitative analyses of bedrock fault surface morphology is an effective method to study faulting history and identify paleo-earthquake. The 2D fractal dimension on a fault surface calculated by isotropic empirical variogram shows vertical segmentation, and the characteristic fractal dimension of each fault surface segment increases step by step from the bottom to the top. This kind of step increase suggests that those fault surfaces are cropped out intermittently likely due to periodic faulting earthquakes. Therefore, the exposure duration or the occurrence time of an earthquake can be inferred by using the characteristic fractal dimension of each fault surface segment, and the vertical co-seismic displacement by using the width of fault surface segment. Based on the quantitative morphologic analyses of the fault (scarp) surfaces on the Huoshan piedmont fault, we indentified three earthquake events, the Hongdong M 8.0

earthquake of 1303 and other two previous earthquakes. Combined with the occurrence times of two pre-historical earthquakes estimated by trenching study, we got an empirical relationship between the characteristic fractal dimension and the occurrence time of earthquake displacement of characteristic faulting earthquake on the Huoshan piedmont fault has also been estimated to be 3-4 m. Moreover, 0.1-0.3 m wide gap between two adjacent fault surface segments, which fractal dimensions increase gradually as fault height increases, is produced by erosion between two earthquakes.

Acknowledgements

This paper has greatly benefited from constructive and helpful comments by an anonymous reviewer. This research was supported by the National Natural Science Foundation of China (grant number: 41372210 and 40872128) and Basic Research Fund from Institute of Geology, China Earthquake Administration (grant number: IGCEA1416 and IGCEA1113).

References

1 Arrowsmith, J.R., 2007. Structural geology, tectonic geomorphology, and recent slip history of the south-central San Andreas Fault. Geological Society of America Annual Meeting, Paper No. 155-3.

2 Benedetti L, Finkel R, Papanastassiou D, et al., 2002. Post-glacial slip history of the Sparta fault (Greece) determined by 36Cl cosmogenic dating: Evidence for non-periodic earthquakes. Geophysical Research Letters, 29(8), 87-1-87-4.

3 Brodsky, E.E., Gilchrist, J.J., Sagy, A., Collettini, C., 2010. Fault smooth gradually as a function of slip, Earth and Planetary Science Letters, 302, 185-193.

4 Brown, R.N. 1987. Fluid flow through rock joins: The effect of surface roughness, J.Geophys.Res., 92, 1337-1347

5 Brown, S.R., and Scholz, C.H. 1985. Broad bandwidth study of the topography of natural rock surfaces, J. Geophys. Res., 90, 2575-2582.

6 Burrough P A. Fractal dimensions of landscapes and other environmental data. Nature, 1981, 294(5838), 240-242.

7 Candela, T., Renard, F., Bouchon, M., Marsan, D., Schmittbuhl, J., Voisin, C., 2009. Characterization of Fault Roughness at Various Scales: Implications of Three-Dimensional High Resolution Topography Measurements, Pure and Applied Geophsics, 166, 1817~1851.

8 Colman, S. M., and Pierce, K. L., 1986. Glacial sequence near McCall, Idaho: Weathering rinds, soil development, morphology, and other relative-age criteria. Quaternary Research, 25(1), 25-42.

9 Davies, S., Hall, P., 1999. Fractal analysis of surface roughness by using spatial data. Journal of the Royal Statistical Society: Series B (Statistical Methodology), 61(1), 3-37.

10 Galli P., Galadini F., Pantosti D., 2008. Twenty years of paleoseismology in Italy, Earth Sciences Reviews, 88, 89-117, doi:10.1016/j.earscirev.2008.01.001.

11 Galli P. and Bosi V., 2003. Catastrophic 1638 earthquakes in Calabria (southern Italy): New insight from paleoseismological investigation, J. Geophys. Res., 108, B1 10.1029/2002JB01713.

12 Galli P., Bosi V., Piscitelli S., Giocoli A., Scionti V., 2006. Late Holocene earthquakes in southern Apennines: paleoseismology of the Caggiano fault, Int. J. of Earth Sciences, 95, 855-870

13 Galli P., Spina V., Ilardo I., Naso G., 2010. Evidence of active tectonics in southern Italy: the Rossano Fault (Calabria), in: Guarnieri P. (ed.) Recent Progress on Earthquake Geology, Nova Scientific Publisher Inc., New York, 49-78.

14 Galli P., Messina P., Giaccio B., Peronace E., Quadrio B., 2012. Early Pleistocene to Late Holocene activity of the Magnola Fault (Fucino Fault System, central Italy), Bollettino di Geofisica Teorica ed Applicata, 53, 435-458.
15 Galli P., Peronace E., 2014. New paleoseismic data from the Irpinia Fault. A different seismogenic perspective for southern Apennines (Italy), Earth-Science Reviews, 136, 175-201.
16 Giaccio B., Galadini F., Sposato A., P. Messina, M. Moro, M. Zreda, A. Cittadini, S. Salvi, A. Todero, 2002. Image processing and roughness analysis of exposed bedrock fault planes as a tool for paleoseismological analysis: results from the Campo Felice fault (central Apennines, Italy). Geomorphology, 49, 281-301
17 Gneiting, T., Ševčíková, H., Percival, D. B., 2012. Estimators of fractal dimension: Assessing the roughness of time series and spatial data.Statistical Science, 27(2), 247-277.
18 Hilley G E, Young J J., 2008. Deducing paleoearthquake timing and recurrence from paleoseismic data, Part I: Evaluation of new Bayesian Markov-Chain Monte Carlo simulation methods applied to excavations with continuous peat growth. Bulletin of the Seismological Society of America, 98(1), 383-406.
19 Klinkenberg B., Goodchild M. F., 1992. The fractal proprieties of topography: A comparison of methods. Earth Surface Processes and Landforms, 17, 217-234.
20 Liu Zhengrong, MengFanxing, 1975. Discussion how to study the relationship between modern tectonic movement and earthquakes in Linfen Basin using the archaeological method. Chinese Journal of Geophysics, 18(2), 127-135 (in Chinese with English abstract)
21 Mandelbrot, B. B., 1975. Stochastic models for the Earth's relief, the shape and the fractal dimension of the coastlines, and the number-area rule for islands. Proceedings of the National Academy of Sciences, 72(10), 3825-3828.
22 Mandelbrot, B. B., 1983. The fractal geometry of nature/Revised and enlarged edition. New York, WH Freeman and Co., 1983, 495
23 Manighetti, I., Boucher, E., Chauvel, C., Schlagenhauf, A., & Benedetti, L., 2010. Rare earth elements record past earthquakes on exhumed limestone fault planes. Terra Nova, 22(6), 477-482.
24 Mayer L., 1984. Dating Quaternary fault scarps formed in alluvium using morphologic parameters. Quaternary Research, 22(3), 300-313.
25 McCalpin, J., 2009. Paleoseismology, 2nd edition International Geophysics vol. 95. San Diego Academic Press, Elsevier Inc., pp. 0074–6142 (613 pp.).
26 Mitchell S G, Matmon A, Bierman P R, et al., 2001. Displacement history of a limestone normal fault scarp, northern Israel, from cosmogenic 36Cl. Journal of Geophysical Research: Solid Earth (1978–2012), 106(B3), 4247-4264.
27 Mouslopoulou, V., Moraetis, D., &Fassoulas, C., 2011. Identifying past earthquakes on carbonate faults: Advances and limitations of the ‘Rare Earth Element’method based on analysis of the Spili Fault, Crete, Greece. Earth and Planetary Science Letters, 309(1), 45-55.
28 Parsons, T., Toda, S., Stein, R.S., Barka, A., Dieterich, J.H., 2000. Heightened odds of large earthquakes near Istanbul: an interaction-based probability calculation. Science 288, 661–665.
29 Polidori L., Chorowicz J., Guillande R., 1991. Description of terrain as a fractal surface, and application to Digital Elevation Model quality assessment. Photogrammetric Engineering & Remote Sensing, 57, 1329-1332.
30 Power, W. L., Tullis, T. E. Weeks, J. D.,1988. Roughness and Wear During Brittle Faulting, Journal of Geophysical Research 93(B12), 15268-15278
31 Power, W.L., Tullis, T. E., Brown, S. R., Boitnott, G. N., and Scholz, C.H.1987. Roughness of natural fault surfaces, Geophys. Res. Lett., 14, 29-32.
32 Power, W.L., Tullis, T.E. 1991. Euclidean and fractal models for the description of rock surface-roughness, Journal of Geophysical Research 96, 415-424.
33 Yongkang Ran, Lichun Chen, Jie Chen, Hu Wang, Guihua Chen, Jinhui Yin, Xiang Shi, Chenxia Li, Xiwei Xu, 2010. Paleoseismic evidence and repeat time of large earthquakes at three sites along the Longmenshan fault zone, Tectonophysics, 491: 141-153.
34 Renard, F., C. Voisin, D. Marsan, and J. Schmittbuhl, 2006. High resolution 3D laser scanner measurements of a strike-slip fault quantify its morphological anisotropy at all scales, Geophys. Res. Lett., 33, L04305, doi:10.1029/2005GL025038.
35 Renard, F., Mair, K., Gundersen, O., 2012. Surface roughness evolution on experimentally simulated faults. J. Struct. Geol. 45, 101–112.

36 Sagy A., Brodsky, E. E., Axen, G. J., 2007. Evolution of fault-surface roughness with slip, Geology 35, 283-286.
37 Sagy, A., and E. E. Brodsky .2009. Geometric and rheological asperities in an exposed fault zone, J. Geophys. Res., 114,B02301, doi:10.1029/2008JB005701.
38 Schlagenhauf, A., Gaudemer, Y., Benedetti, L., Manighetti, I., Palumbo, L., Schimmelpfennig, I., ...&Pou, K., 2010. Using in situ Chlorine-36 cosmonuclide to recover past earthquake histories on limestone normal fault scarps: a reappraisal of methodology and interpretations. Geophysical Journal International, 182(1), 36-72.
39 Schlagenhauf A., 2009. Identification des forts séismes passés sur les failles normales actives de la région Lazio-Abruzzo (Italie Centrale) par ?datations cosmogéniques' (36Cl) de leurs escarpements, PhD thesis, Universitè Joseph-Fourier, Grenoble I.
40 Stewart I., 1996. A rough guide to limestone fault scarps. Journal of Structural Geology, 18(10): 1259-1264
41 Stewart, I.S., 1993. Senitivity of fault-generated scarps as indicators of active tectonism: some constrains from the Aegean region, LandScape sensitivity (edited by Thomas, D.S.G. &Allison,R.J.).129-147, Wiley, Chichester.
42 Sung, Q. C., Chen, Y. C., & Chao, P. C., 1998. Spatial variation of fractal parameters and its geological implications. TAO, 9(4), 655-672.
43 Sung, Q. C., Chen, Y. C., 2004. Self-affinity dimensions of topography and its implications in morphotectonics: an example from Taiwan. Geomorphology, 62(3), 181-198.
44 Wallace R E., 1981. Active faults, paleoseismology, and earthquake hazards in the western United States. Earthquake prediction, 209-216.
45 Wallace R.E., 1984. Fault scarps formed during the earthquake of October 2, 1915, Pleasant Valley, Nevada and some tectonic implications. U. S. Geol. Surv. Prof., 1274-A
46 Wang Nailiang, Yang Jingchun, Xia Zhengkai, 1996. Cenozoic sedimentary and tectonic geomorphology in Shanxi graben system. Beijing: Science Press, 1-392 (in Chinese with English abstract)
47 Wei Zhanyu, Honglin He, Feng Shi, Xiang Gao, Changpeng Xu, 2010. Topographic Characteristics of Rupture Surface Associated with the 12 May 2008 Wenchaun Earthquake. BSSA, 100(5B): 2669–2680, doi: 10.1785/0120090260
48 Wei, Z. and He, H., 2013. Weathering history of an exposed bedrock fault surface interpreted from its topography. Journal of Structural Geology, 56, 34-44.
49 Wen Xueze, 2000. Influence of the great 1303 earthquake rupture, Shanxi, on earthquake recurrence behavior of its adjacent fault segments. Earthquake Research in China, 16(1): 22-27.
50 Wiatr, T., Papanikolaou, I., Fernández-Steeger, T., &Reicherter, K., 2015. Bedrock fault scarp history: Insight from t-LiDAR backscatter behaviour and analysis of structure changes. Geomorphology, 228, 421-431.
51 XieXinsheng, Jiang Wali, Wang Huanzhen, Feng Xiying, 2004. Holocene activity on the Taigu fault and its relationship to 1303 Hongtong M8 earthquake. ActaSeismologicaSinica. 26(3): 281-293
52 Xu T, Moore I D, Gallant J C., 1993. Fractals, fractal dimensions and landscapes-a review. Geomorphology, 8(4): 245-262.
53 Xu Xiwei, Deng Qidong, 1990. The features of the Late Quaternary activity of the piedmont fault of Mt. Huoshan, Shanxi Province and 1303 Hongdong earthquake (Ms=8). Seismology and Geology, 1: 21-30 (in Chinese with English abstract)
54 Xu Xiwei, Deng Qidong, Han Zhujun. 1993. The late Quaternary activity of the piedmont fault of Mt. Huoshan and paleoearthquake study. In: Ma Zongjin (ed). Earthquake Research and Systematical Disaster Reduction in Linfeng, Shanxi. Seismological Press, Beijing. 136-148 (in Chinese with English abstract)
55 Xu Yueren, 2013. A Study on the Faulting Characteristics of the Huoshan Piedmont Fault, Shanxi Province, China, in the Late Quaternary. Ph.D. Thesis of Institute of Geology, China Earthquake Administration (in Chinese).
56 Young, J. J., J R. Arrowsmith, L. Colini, L. Grant, and B. Gootee, 2002. Three-dimensional excavation and recent rupture history along the Cholame segment of the San Andreas fault, Bull. Seismol. Soc. Am. 92, no. 7, 2670–2688, doi 10.1785/0120000604.
57 Zhang Y Q, Mercier J L, Vergély P., 1998. Extension in the graben systems around the Ordos (China), and its contribution to the extrusion tectonics of south China with respect to Gobi-Mongolia. Tectonophysics, 285(1-2): 41-75
58 Zreda M, Noller J S, 1998. Ages of prehistoric earthquakes revealed by cosmogenic

chlorine-36 in a bedrock fault scarp at Hebgen Lake. Science, 282(5391): 1097-1099.

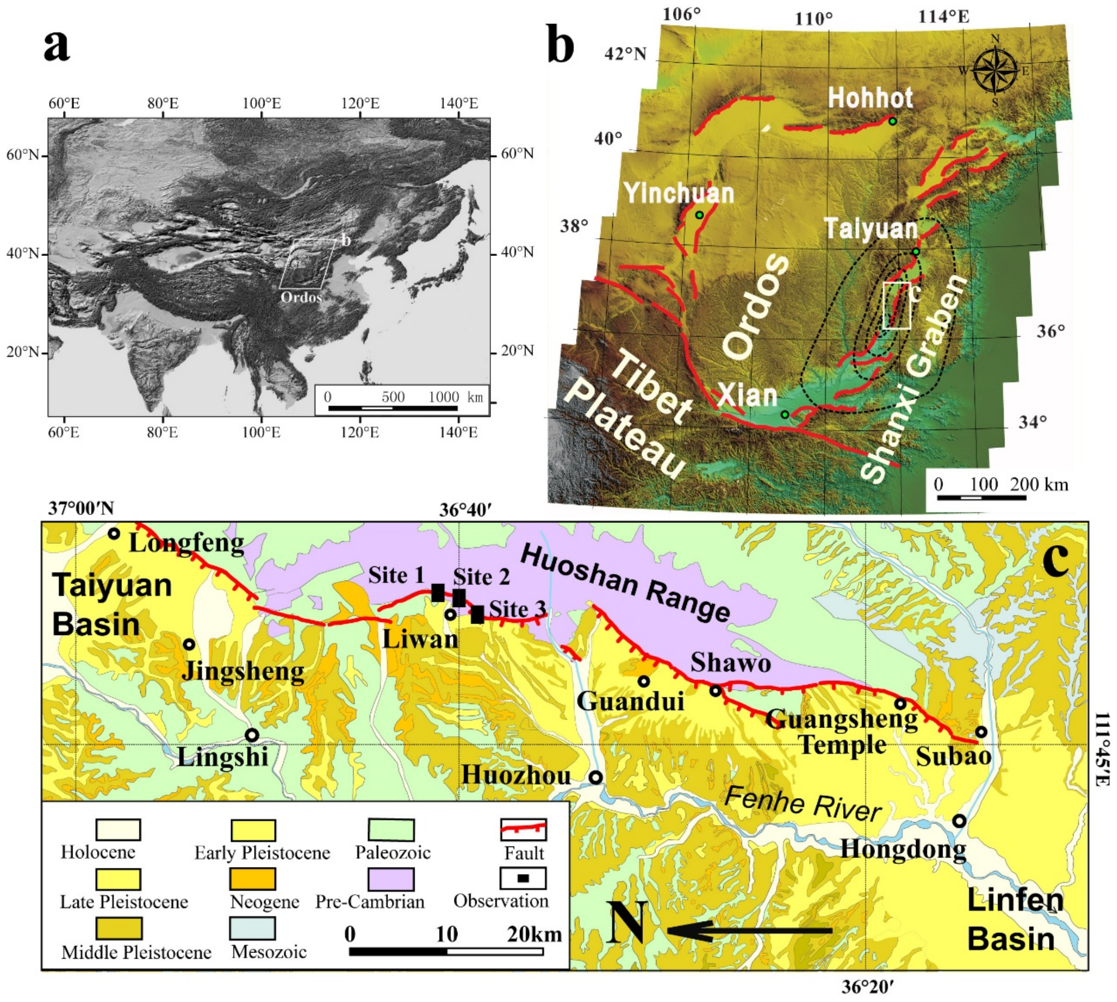

Figure 1 Geologic map of the Huoshan piedmont fault. a, location of the Ordos block within north-central China. b, Active faults surrounding the Ordos block. The background is a color shaded-relief view of SRTM elevation data, the red lines are active faults (from Deng et al., 2007), the black dashed lines are isoseismals of the Hongdong M 8 earthquake of 1303 (Earthquake Engineering Investigation Institute of Shanxi Province, 2009), and the white rectangle shows the location of Figure 1c. c, Geometry of the Huoshan piedmont fault. Black rectangles show the locations of scanned fault scarps. Other geologic information is shown in the legend.

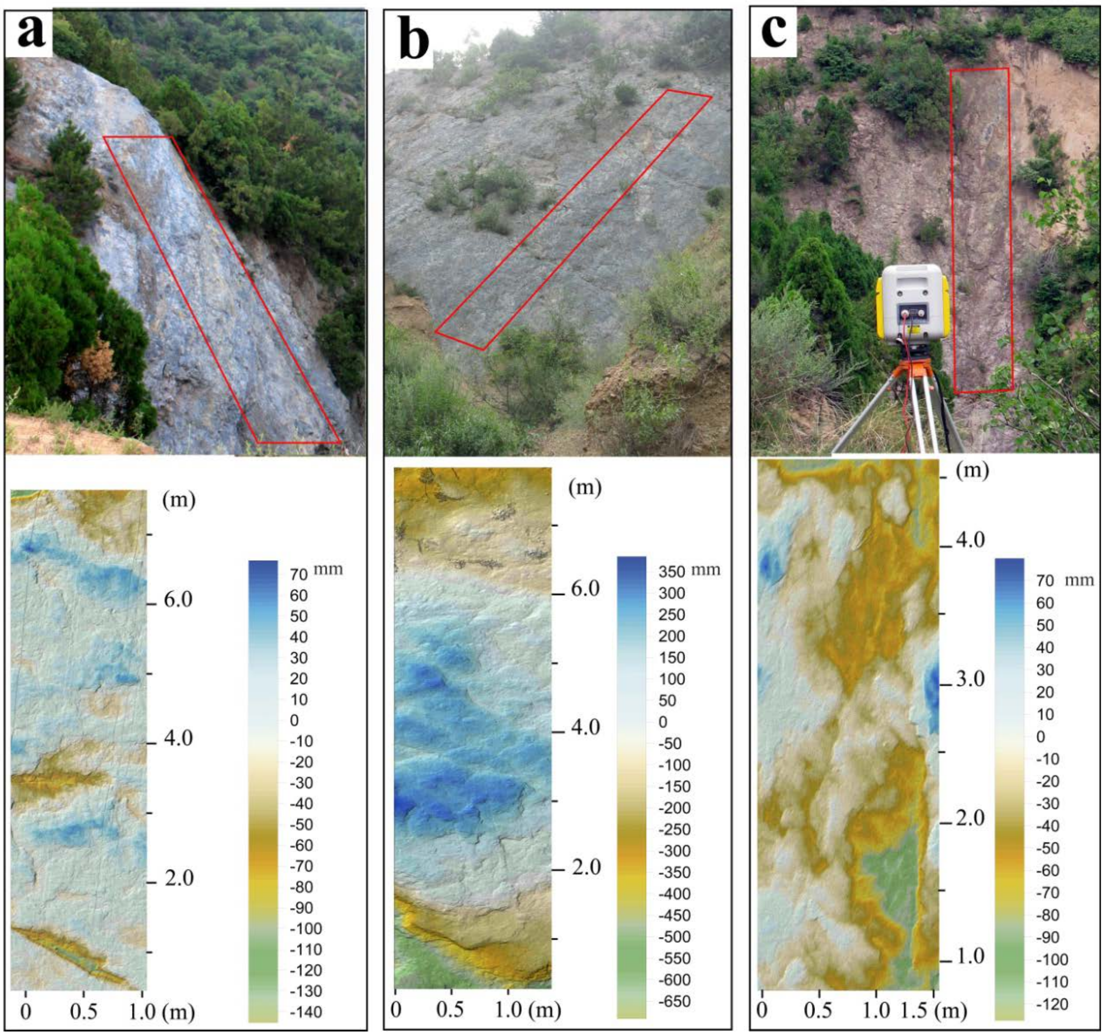

Figure 2 Fault outcrops (upper) and their rendering morphology derived from scanned point clouds (below). a, b and c are three fault surface outcrops, whch locations are indicated by Site 1, Site 2 and Site 3 in Figure 1c, as well as the scan locations (red rectangles). Panels show the morphologies of the three fault surfaces, respectively.

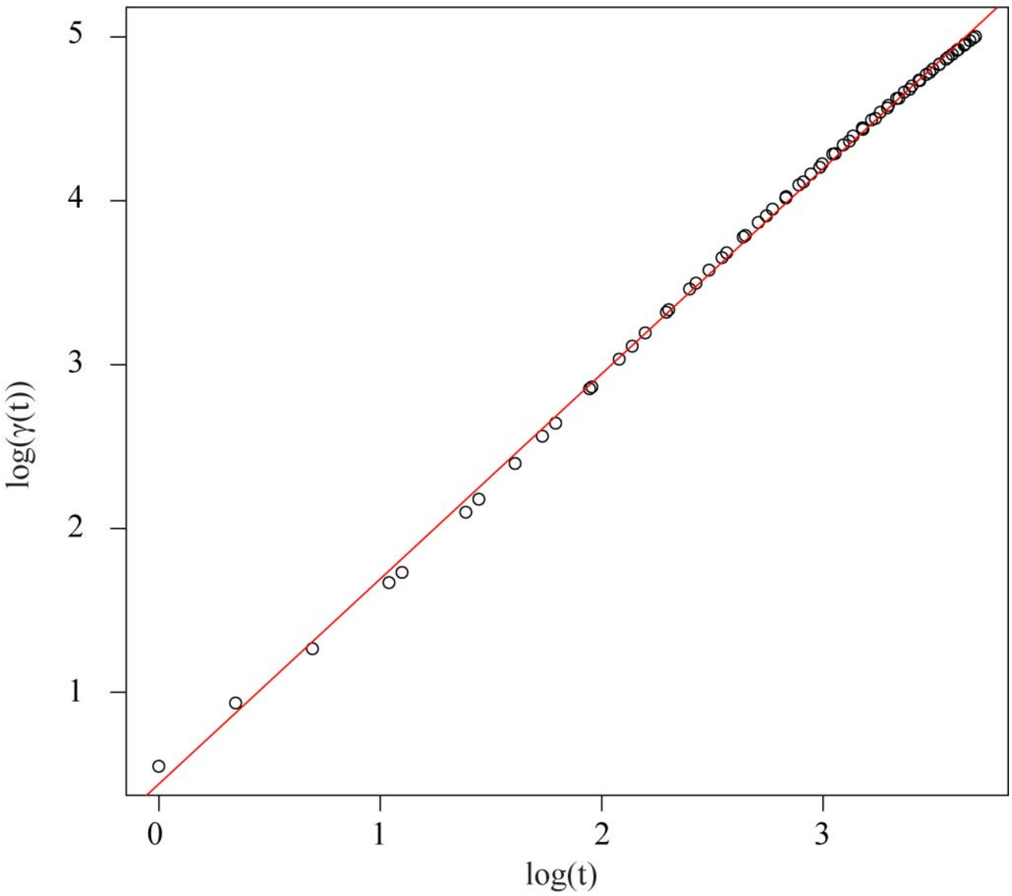

Figure 3 Log-log regressions for the isotropic variogram each dot represents the covariance of points with a certain separation distance *t* ; red line is the linear fitting of the dots, and its slope is linearly associated with the fractal dimension of 2D spatial data.

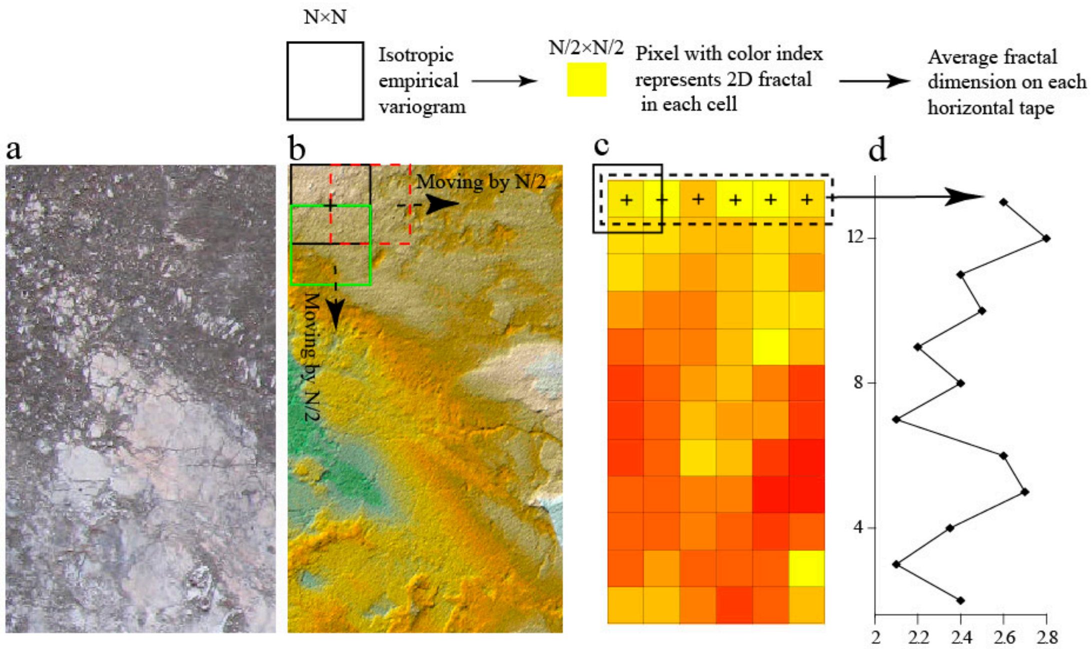

Figure 4 Schematic diagram for calculating fractal dimension of fault surface. (a) Photo of the fault surface; (b) Hillshade image created by the high resolution digital elevation model of scanned surface; the colored squares stand for the moving windows with size of N×N in both directions of horizontal and vertical; (c) shows image of fractal dimension for fault surface; each pixel stand for the estimator of fractal dimension for surface cell with size of N/2×N/2; the yellow-red colors are index of fractal value; (d) the diagram shows the fractal values distribution of fault surface along with vertical height; each black point is the average fractal dimension on each horizontal row.

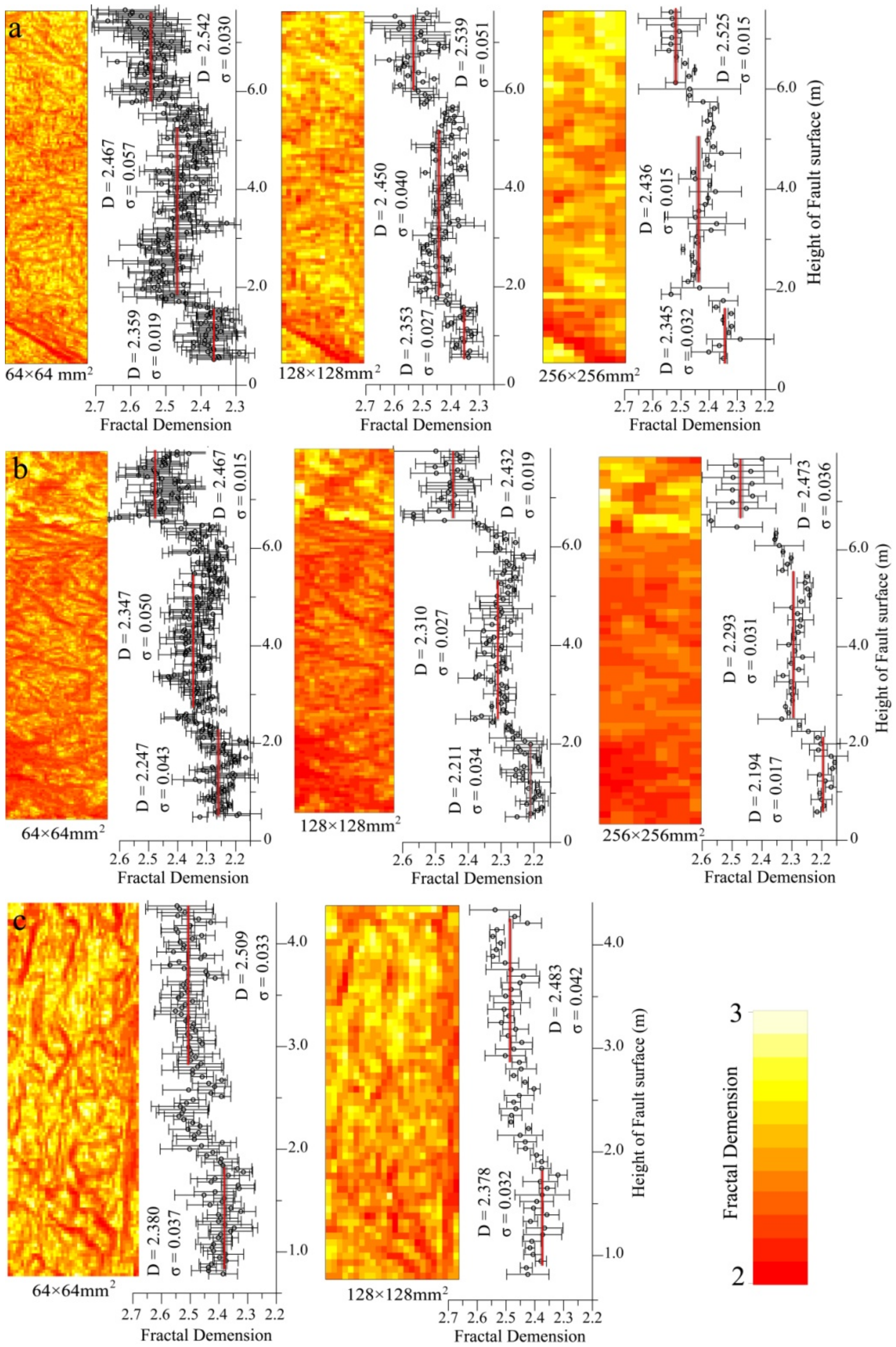

Figure 5 Raster images of fractal dimension and corresponding average fractal along surface height for fault surfaces. a, b and c correspond to the three scanned bedrock fault surface. In each panel, the raster images with color range from red to light yellow (left) show the spatial distribution of fractal dimensions on the fault surface, while the scatter diagrams (right) show the variability of the average fractal along the surface height. The raster images are generated by three types of moving window, 64×64 mm^2, 128×128 mm^2 and 256×256 mm^2 from left to right. Black dots with error bars are the mean value of each horizontal row in the fractal raster images and gray error bars represent 95% confidence interval. The red vertical bars show the average value for each group of samples (see text for details).

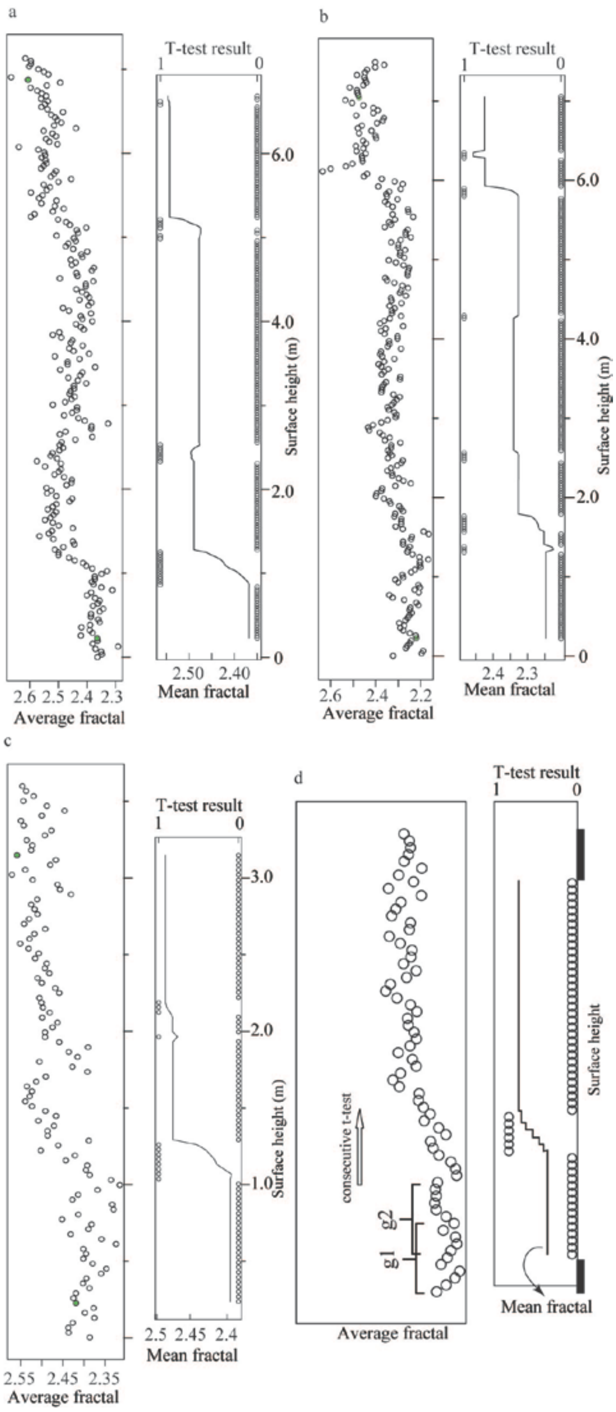

Figure 6. Results of determination of weathering bands applying Student's *t*-test. (a), (b) and (c) show the weathering bands on surface a, surface b and surface c, respectively, based on the fractal derived by using the moving window of 64×64mm^2. (d) Shows a simplified sketch of the process using two-sample Student's *t*-test to quantitatively determine the bands. "g1" and "g2" indicate two adjacent data sets of *n* data points, which overlapped each other in a half of data points (*n/2*), standing for two surface segments. Dots assigned by 0 or 1 on right plots are the *t*-test result, and detailed description is showed in section 5.1; each straight segment on the mean fractal curve indicate one weathering band on fault surface.

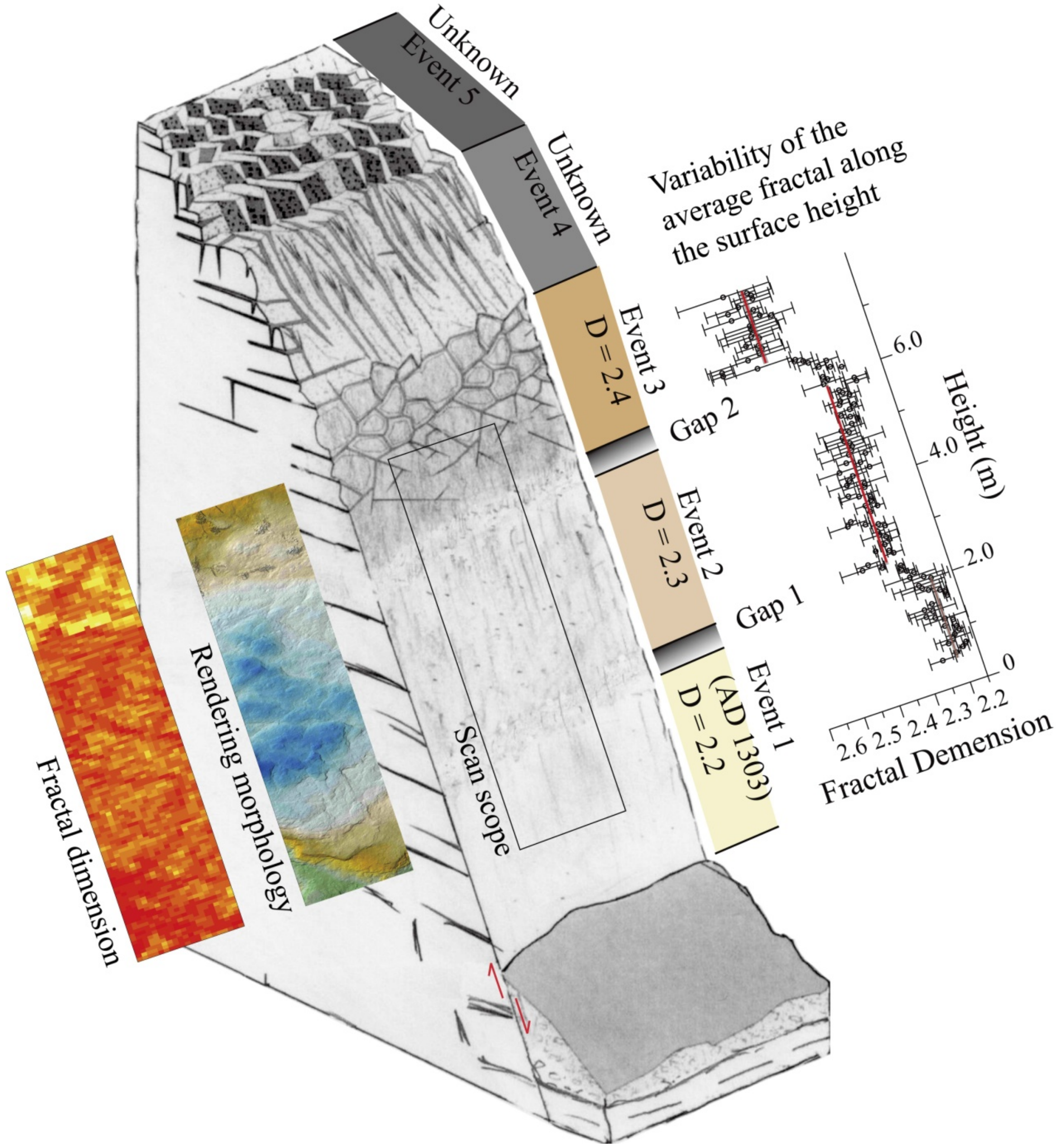

Figure 7 Evolutionary model of fault scarp surface, showing five weathering bands corresponding to five different exposure times (modified from model of Giaccio et al, 2002). The two higher bands have conspicuous weathering morphological feature identified by naked eye easily; while the three lower bands have no conspicuous weathering morphological feature identified by naked eye, and similar dip angle as original fault dip angle. The quantitative morphology applied in our study can identify the three lower bands. The rectangle on the fault scarp surface shows the scan scope, and the two color rectangles on the left show fractal dimension and rendering morphology, respectively. The characteristic fractal of the three lower bands are demonstrated by color bars and scatter diagrams on the right.

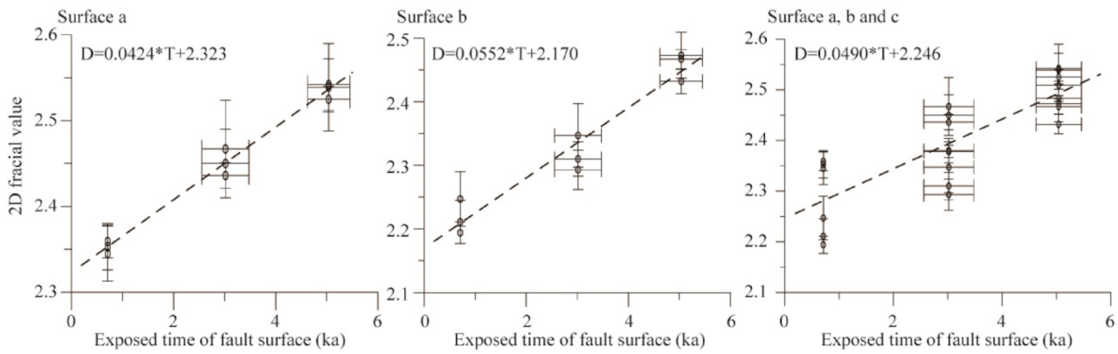

Figure 8 Fitting lines of relationship between 2D fractal dimension and exposure time. The gray belts show the time spans of paleo-earthquake occurrence. The three empirical relations, are all fitted based on the characteristic fractal dimensions derived by using the moving window of 64×64mm^2.